JOURNAL OF THERMOPHYSICS AND HEAT TRANSFER
Vol. 17, No. 2, April–June 2003

# Electron Density Measurements Behind Strong Shock Waves by H-$\beta$ Profile Matching

Kazuhisa Fujita,* Sunichi Sato,† and Takashi Abe‡
*Institute of Space and Astronautical Science, Kanagawa 229-8510, Japan*
and
Hirotaka Otsu§
*University of Tokyo, Tokyo 113-8654, Japan*

**Emission spectroscopy was performed in a free-piston double-diaphragm shock tube to measure the electron density behind a strong shock wave, using nitrogen as the test gas. Time-frozen spectra from behind the shock wave were taken by an image-intensified charge-coupled device camera with a gate width of 100 ns. The laser schlieren diagnostics was used to detect the shock arrival and to correlate observed spectra with the distance from the shock front accurately. The electron density was measured by means of a line profile matching technique, using the H-$\beta$ line broadened by the Stark effect. Using this measurement system, the electron density distribution was obtained with a high spatial resolution of $\pm 0.6$ mm at a shock velocity of 12 km/s. Experimental results show that, especially at high shock velocities, the measured electron density increases more quickly behind the shock front than predicted by the thermal and chemical nonequilibrium models widely used. Several drawbacks in the conventional ionization model at high shock velocities are pointed out.**

## Nomenclature

| | | |
|---|---|---|
| $L$ | = | distance from the shock front, mm |
| $n_e$ | = | electron number density, m$^{-3}$ |
| $P_0$ | = | ambient pressure ahead of the shock wave, torr |
| $T$ | = | translational-rotational temperature of heavy species, K |
| $T_v$ | = | vibrational-electronic temperature, K |
| $V$ | = | incident shock velocity, km/s |
| $\lambda$ | = | wavelength, nm |
| $\Phi(\lambda)$ | = | slit function defined in Eq. (1), nm$^{-1}$ |

## Introduction

NONEQUILIBRIUM aerothermodynamics behind a strong shock wave is an important topic to hypersonic flight and reentry because the nonequilibrium thermochemical phenomena affect the aerodynamic characteristics and the heating rate of hypersonic vehicles significantly. To understand such nonequilibrium phenomena, many thermochemical models have been developed[1–4] and applied to assess the flight environments of hypersonic vehicles and reentry capsules. The parameters in these models are adjusted to numerically reproduce the flight environments encountered during the reentry from the low Earth orbit. Consequently, numerical predictions show good agreement with the data from several flight and ground experiments where the shock velocities lie below about 10 km/s (Ref. 5).

To extend the model applicability to a higher velocity range, such as the Earth reentry of the MUSES-C sample return capsule[6] at a reentry velocity of more than 12 km/s, it is necessary to assess the accuracy of the existing thermochemical models in the higher velocity range and to modify them so that they can reproduce the experimental data. However, the numerical models have not been verified adequately in such a high velocity range because of the experimental difficulties. For this reason, we embarked on measurement of the physical properties behind a strong shock wave in order to increase the database that can be used for assessment and improvement of the physical models. In a previous work[7] we developed a spectroscopic technique to measure the rotational and vibrational temperatures of molecular species and the electronic temperature of atomic species in the nonequilibrium region behind a strong shock wave.

As the shock velocity increases, the molecular species are almost dissociated, and considerable ionization of the atomic species occurs. Because the ionization energy of the atomic species is much higher than the vibrational excitation energy and the dissociation energy of the molecular species, the thermodynamic behavior of the shock layer is affected significantly by the nonequilibrium ionization and recombination processes. Therefore, it is important to use the accurate ionization and recombination models for assessment of the flight environments of the MUSES-C capsule. In the present study we measure the electron density behind a shock wave by using an improved experimental facility. Numerical predictions obtained by the widely used ionization and recombination models are compared with the experimental results.

The electrical probe is a popular tool to measure the electron density and the electron temperature simultaneously when the electron density is not too high.[8] However, when the plasma is moving at a high speed the probe measurement becomes difficult and often inaccurate because of the contribution of the directed velocity to the total velocity of charged particles in the vicinity of the probe.[8] Although microwave diagnostic techniques are free from this difficulty, their spatial resolution is very poor. To avoid these difficulties, we measure the electron density by emission spectroscopy, using the H-$\beta$ line profile as the spectral indicator of the electron density.

## Experimental Setup

Experimental investigations were conducted using a free-piston double-diaphragm shock tube at the Institute of Space and Astronautical Science.[7] The shock tube can generate a strong shock wave at the maximum velocity of 14 km/s in the ambient air of 0.3 torr ahead of the shock wave, which covers the MUSES-C reentry condition. The original test section of the stainless-steel shock tube

---

Received 29 April 2002; revision received 15 August 2002; accepted for publication 16 August 2002.

*Research Associate, Research Division for Space Transportation; kazu@kazudom.eng.isas.ac.jp. Member AIAA.

†Technical Staff, Research Division for Space Transportation.

‡Professor, Research Division for Space Transportation. Senior Member AIAA.

§Graduate Student, Faculty of Engineering, Department of Aeronautics and Astronautics; currently Research Associate, Shizuoka University, Department of Mechanical Engineering, Shizuoka 432-8561, Japan. Member AIAA.

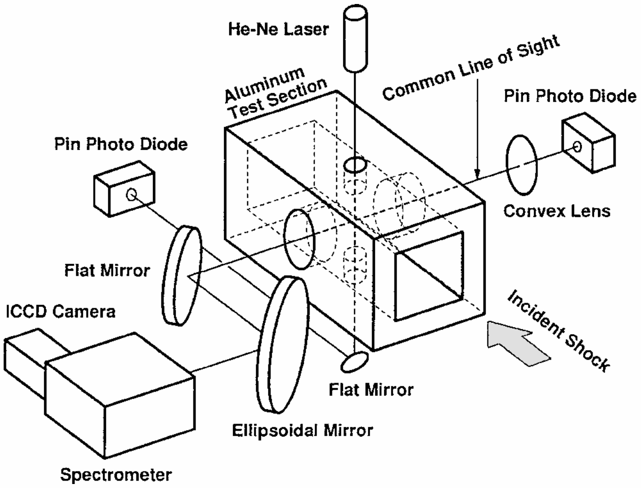

**Fig. 1 Experimental setup of test section.**

has been replaced with the one made of aluminum alloy in order to reduce the emission from impurities, consisting mostly of iron.[4] The flow channel of the test section is 35.4-mm square in cross section. The shock velocity is measured by three pressure sensors, which are aligned in the direction of the shock-tube axis, calibrated by the laser schlieren measurement.[7] The uncertainty associated with the shock velocity measurement is estimated to be less than ±1%.

Figure 1 illustrates the experimental setup of the test section, which was originally developed for the measurement of the rotational, the vibrational, and the electronic excitation temperatures.[7] Quartz windows are installed on four sides of the flow channel to let the laser beam pass through the test gas and to observe the light emitted from behind the shock wave. During the experiment, the laser schlieren diagnostics, the emission spectroscopy, and the total radiation intensity measurement are conducted simultaneously.

### Laser Schlieren Diagnostics

In the previous study[7] we found that laser schlieren diagnostics was a simple and effective approach to detect the arrival of the shock wave even when the shock velocity was extremely high and the pressure ahead of the shock wave was low. The present setup is an improved version of the preceding setup; with the new setup the measured spectra can be correlated with the distance from the shock front more accurately. As shown in Fig. 1, a He-Ne laser beam with a 0.6-mm-beam diameter is aligned to pass through the test gas perpendicularly to the axis of the shock-tube flow. Deflection of the beam as a result of a density gradient at the shock front causes a change in the output signal of an avalanche pin photodiode (APD, Hamamatsu Photonics S2383), which has a photosensitive surface of 1.0 mm in diameter, a spectral response of 400–1000 nm, and 10 ns rise-and-fall times.

### Time-Frozen Spectroscopy

To eliminate the chromatic aberration, a flat and an ellipsoidal mirror are used to focus the field of the radiating gas on the entrance slit of the spectrometer, as illustrated in Fig. 1. The entrance slit is set perpendicularly to the axis of the shock-tube flow so that an emission image parallel to the shock wave can be obtained. This linear image is then separated into its spectral components by an imaging spectrometer (ORIEL MS127i), which generates a two-dimensional image (distance along the slit in one dimension and wavelength in the other dimension) on the photosensitive surface of an image-intensified charge-coupled device (ICCD) camera (ANDOR InstaSpecV IS510) attached to the spectrometer. A mean spectrum is obtained by accumulating spatial components for each wavelength because we can assume a good uniformity along the direction parallel to the shock wave in the central region of the flow channel.[7]

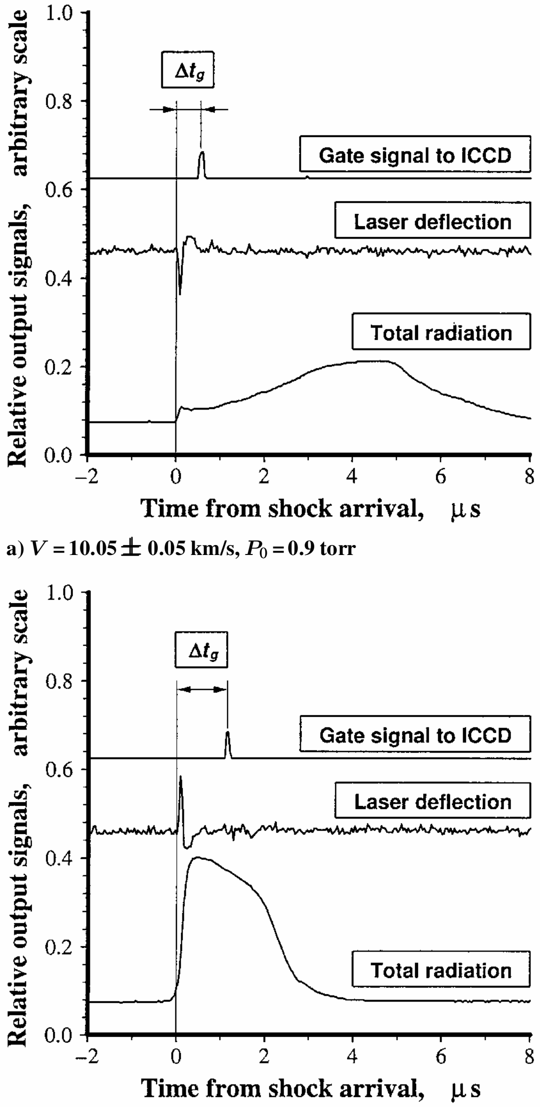

a) $V = 10.05 \pm 0.05$ km/s, $P_0 = 0.9$ torr

b) $V = 12.55 \pm 0.05$ km/s, $P_0 = 0.3$ torr

**Fig. 2 Output signals of APD and gate signal to ICCD.**

The line of sight from the spectrometer is aligned perpendicularly to the axis of the shock-tube flow and made to intersect the laser beam perpendicularly at the center of the flow channel section. The ICCD camera is gated by a pulse generator (Stanford Research Systems DG-535) with a gate width of 100 ns. The trigger timing of the ICCD camera is controlled according to an output signal of a pressure sensor located 40.0 mm upstream of the position of sight. The distance from the shock front, at which a spectrum is taken by the ICCD camera, can be determined by multiplying the measured shock velocity by the delay time of this gate signal from the shock arrival $\Delta t_g$ (see Figs. 2a and 2b). This setup allows us to obtain a time-frozen spectrum at any desired distance from the shock front with ±0.6 mm spatial accuracy when the shock velocity is 12 km/s. The spatial distribution of the spectra is obtained by repeating the measurement at different trigger times for the ICCD camera, maintaining the shock velocity at a fixed value.

### Total Radiation Intensity Measurement

Because we determine the electron density distribution by a repetitive measurement just described, reproducibility of each run in the shock-tube facility is essential in obtaining an accurate result. In general, the shock velocities are not exactly the same, and the test gas behind the shock wave is sometimes disturbed unintentionally by the strong deformation of the contact surface, which can originate from the irregularity in diaphragm rupture. To cope with these problems, the total radiation intensity is also measured by another APD having the same performance as that used for the laser schlieren measurement. The line of sight from the APD is aligned with that of the spectrometer, which is indicated as the common line of sight in Fig. 1.

In the beginning of the experiment, for each shock velocity we examined the uniformity of the field of the radiating gas behind the shock wave by taking photographs and selected the standard profiles of pressure and total radiation intensity behind the shock wave. Among a large number of measurements, we identified the runs with good reproducibility by comparing the profiles of pressure and total radiation intensity, in addition to the measured shock velocity. Based on the results of the previous study,[7] the runs with deviation higher than ±0.5% in the shock velocity from the target velocity were excluded. In this way the results with good reproduction were selected and used to determine the electron density distribution for each shock velocity.

### Test Gas and Impurities

In the present experiment pure nitrogen was used as the test gas in order to make the physical process less complicated and to reduce the radiation from impurities contained in the ambient air of the test section.[7] Consequently, the emission of the violet system of carbon nitride, which often overlaps the spectrum of our interest undesirably when the ambient air is used, was found to be reduced adequately. The modified test section made of aluminum alloy was found to produce less radiation from impurities than the original stainless-steel shock tube. However, the Balmer lines of atomic hydrogen could not be eliminated completely from observed spectra. Atomic hydrogen can originate from the water vapor, which inevitably adheres to the channel surface when the shock tube is exposed to the atmosphere. For this reason, we could observe the H-$\beta$ line without adding hydrogen intentionally for the purpose of electron density measurement. The H-$\beta$ line was found more luminant than any other Balmer lines observed in the wavelength range of 380–540 nm.

One concern with regard to the water vapor is that it might enhance the electron density behind the shock wave. Because it is difficult to control the concentration of the water vapor, electron density was examined by varying the concentration of hydrogen mixed intentionally with pure nitrogen to a concentration of 0 to 3% in order to assess the influence of atomic hydrogen on the ionization process. Electron density was found clearly not to depend on the concentration of hydrogen in the range of concentration tested. Because the concentration of the water vapor is estimated to be much less than 1% in the present experiment, we consider that the water vapor contained in the test section does not have any influence on the ionization process.

## Experimental Results

### Shock-Front Detection

Typical output signals from the APD are shown in Figs. 2a and 2b for two shock velocities of 10.05 and 12.55 km/s, respectively. In the present laser schlieren setup an increase in density of electrically neutral species at the shock arrival, namely the shock front, is detected by a drop in the output signal of the APD, as seen in Fig. 2a. In contrast, an increase in density of charged species, namely the ionization front, is detected by a rise in the output signal, which is also seen in Fig. 2a immediately behind the shock front. As the shock velocity increases, the rise in the output signal at the ionization front becomes more prominent, and the ionization front approaches the shock front until they finally overlap.[7] This is the case with Fig. 2b, in which only a rise in the output signal is detectable at the shock arrival. Even in this case, because the ionization front is located at the close vicinity of the shock front, the shock front can be detected by the laser schlieren system without losing accuracy.

### Total Radiation Intensity

Figure 2 also shows typical profiles of the total radiation intensity measured by the APD. In both Figs. 2a and 2b the test gas behind the shock front begins to radiate from immediately behind the shock front. For $V = 10.05$ km/s the total radiation intensity is found to increase gradually until 4 $\mu$s after the shock arrival (equivalent to $L \approx 40$ mm). Beyond 5 $\mu$s after the shock arrival ($L \approx 50$ mm), the total radiation intensity begins to decrease because of the encroachment of the contact surface.

In contrast, the total radiation intensity for $V = 12.55$ km/s increases very quickly until 0.4 $\mu$s after the shock arrival ($L \approx 5$ mm) and then decreases gradually until the contact surface arrives at 1.7 $\mu$s after the shock arrival ($L \approx 21$ mm). This gradual decrease is considered to be caused by a decrease in temperature, which is brought about by the radiative energy loss from the test gas. As the shock velocity increases and the pressure decreases, the radiative heat transfer seems to play a more significant role.

### Time-Frozen Spectrum

Time-frozen spectra were obtained in a wavelength range of 477–537 nm with a moderate spectral resolution of 0.16 nm per pixel of the ICCD camera. Typical examples of the H-$\beta$ line and the atomic lines of nitrogen are shown in Figs. 3a and 3b. Radiation from impurities such as iron and carbon, which is often observed in other shock-tube experiments, is not discernible in our results. The H-$\beta$

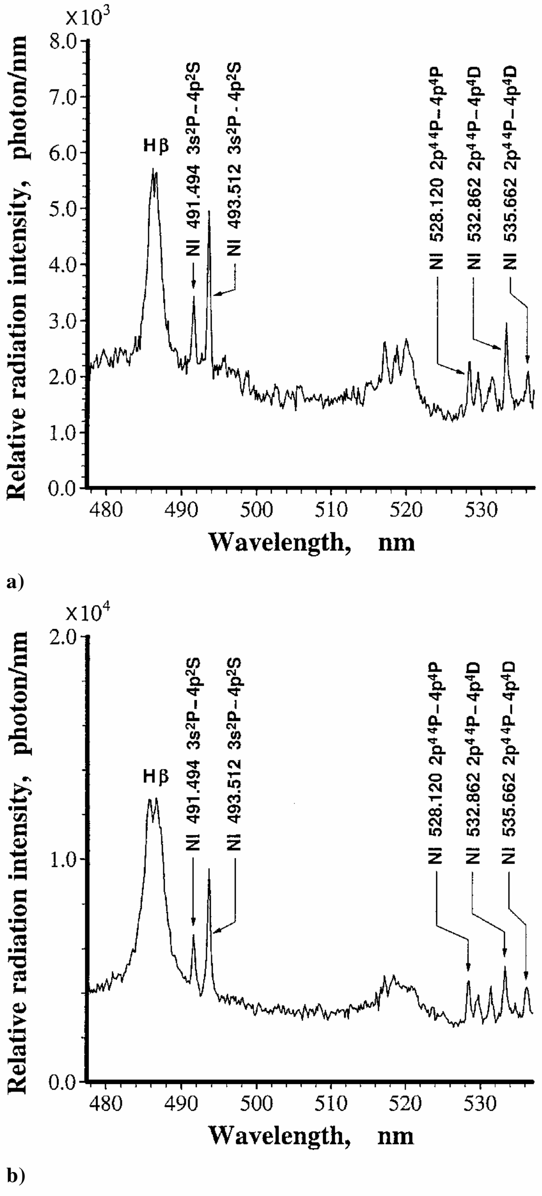

**Fig. 3 Observed H-$\beta$ and atomic-N lines: a) $L = 26.7 \pm 0.5$ mm, $V = 10.05 \pm 0.05$ km/s, $P_0 = 0.9$ torr and b) $L = 6.0 \pm 0.6$ mm, $V = 12.55 \pm 0.05$ km/s, $P_0 = 0.3$ torr; spectral resolution = 0.16 nm/pixel.**

line is found to be the most luminant of all atomic lines in this wavelength range. With the available moderate spectral resolution, the characteristic twin peaks of the H-$\beta$ line broadened and shifted by the Stark effect are recognizable. Even at the lower shock velocity of 10.05 km/s where the electron density is not expected to be high, the full width at half-maximum of the H-$\beta$ line is approximately 2 nm, which is approximately seven times larger than that caused by slit broadening of the spectroscopic system. This clearly shows that the physical broadening process in the plasma is primarily responsible for the observed H-$\beta$ line profile.

## Evaluation of Electron Density

### Line Profile Matching Technique

In the present experiment the Stark broadening of lines, which is strongly correlated with the number density of charged particles, is the dominant broadening mechanism. Profiles of many hydrogen lines broadened by the Stark effect have been precisely calculated by Griem et al.[9] and tabulated in Ref. 10. The H-$\beta$ profile is one of the best known spectral indicators of electron density, which has been studied both experimentally and theoretically in detail.

As a first step, theoretical H-$\beta$ line profiles are computed using Griem's method described in Ref. 10 for electron temperatures from 5,000–40,000 K at every 5000 K and for electron number densities from $10^{21}$ to $10^{23}$ $m^{-3}$ at every $10^{21}$ $m^{-3}$. The resultant 8 × 101 spectra compose a database of the H-$\beta$ line profiles. Figure 4 shows typical profiles calculated for several electron densities and temperatures. In Fig. 4 it is seen that the H-$\beta$ profile is strongly dependent on the electron density and nearly independent of the temperature. Consequently, the electron density can be determined accurately from the observed line profile, whereas the electron temperature cannot be determined definitely by this method.

As a second step, the slit function for the spectroscopic system is determined experimentally and then used to modify the theoretical spectra in the database to incorporate the slit broadening effect. In this study the slit function was determined using an atomic line of Hg I at 404.66 nm (in the atmosphere) emitted from a calibration lamp. For our spectroscopic system it is given by

$$\Phi(\lambda) = \exp[a/(b + \Delta\lambda^2) + c\Delta\lambda^2 + d][nm^{-1}] \qquad (1)$$

$$\Delta\lambda \equiv \lambda - \lambda_c \qquad (2)$$

where $\lambda_c$ is the center wavelength, and

$$a = 1.519226 \times 10^{+00}, \qquad b = 2.914946 \times 10^{-01}$$

$$c = -4.306887 \times 10^{-02}, \qquad d = -4.634297 \times 10^{+00}$$

Figure 5 shows the slit function adjusted to the experimental profile. In reality, because a FWHM of the H-$\beta$ line as a result of the Stark effect was much larger than that of the slit function in the present measurement, incorporation of the slit function was found to have only a minor influence on the determination of the electron density. The numerical spectra in the database are further modified to incorporate the grating efficiency of the spectrometer and the quantum efficiency of the ICCD camera, both of which are a function of the wavelength, so that they can finally simulate the experimental spectra consistently.

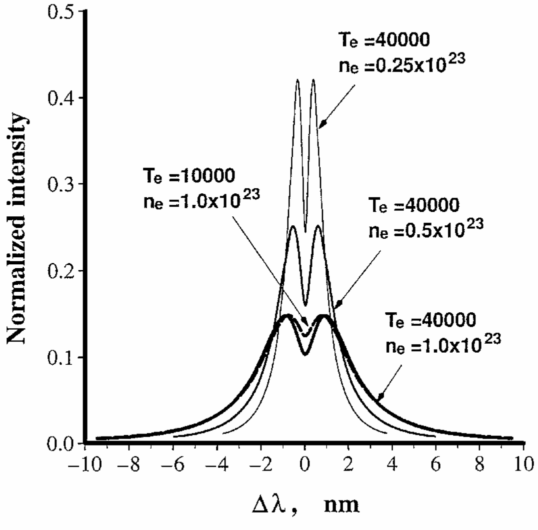

Fig. 4 Calculated H-$\beta$ profile broadened by Stark effect.

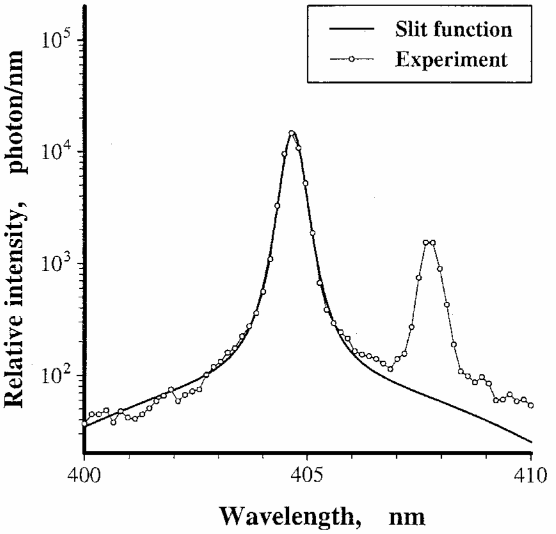

**Fig. 5 Slit function adjusted to experimental profile of a Hg-I line at 404.66 nm; spectral resolution = 0.16 nm/pixel.**

As a final step, the most appropriate numerical profile, which can minimize the root mean square of the difference between the numerical profile and the observed one, is selected from the database. In this way the best-estimated electron density, which gives the best-matched numerical spectrum, is determined for each experimental spectrum.

### Results

Figure 6 shows typical examples of a numerical H-$\beta$ line profile matched with the experimental profile. The numerical profiles are found to be in excellent agreement with the experimental profiles. Because the line profile broadened by the Stark effect is strongly dependent on the electron number density, an estimation error in fitting is reasonably small. For example, a 10% increase in electron number density produces more than a 50% increase in the mean square root of the difference between of the numerical and the experimental profile when $n_e = 10^{22}$ $m^{-3}$. The fitting error is estimated to be less than 1% in general. The major errors in the electron density measurement originate from the approximation used to calculate the primary H-$\beta$ line profile by Griem's method. According to Griem,[10] such errors are expected to be less than ±8% in the present study. Errors in the slit function, the efficiencies of the spectrometer and the ICCD camera, and uncertainty in measured spectral intensity are expected to result in less than ±4% of errors of the electron density. As a whole, the accuracy of the electron density measurement in this study is expected to remain within ±12% of errors in general.

The distribution of the measured electron number density behind the shock front is shown in Figs. 7a, 7b, and 7c for $V = 10.05$, 11.01, and 12.55 km/s, respectively. In general, accuracy of the measured electron density decreases forward of the shock front because radiation intensity of the H-$\beta$ line becomes weaker compared with the background radiation. In the close vicinity of the shock front, intensity of the H-$\beta$ line is no longer sufficient to determine the electron density accurately. In Fig. 7a the electron density is found to increase monotonically with the distance from the shock front. In contrast, the electron density shown in Fig. 7c is almost uniform and increases slowly from 2–5 mm behind the shock front and decreases slightly beyond 5 mm.

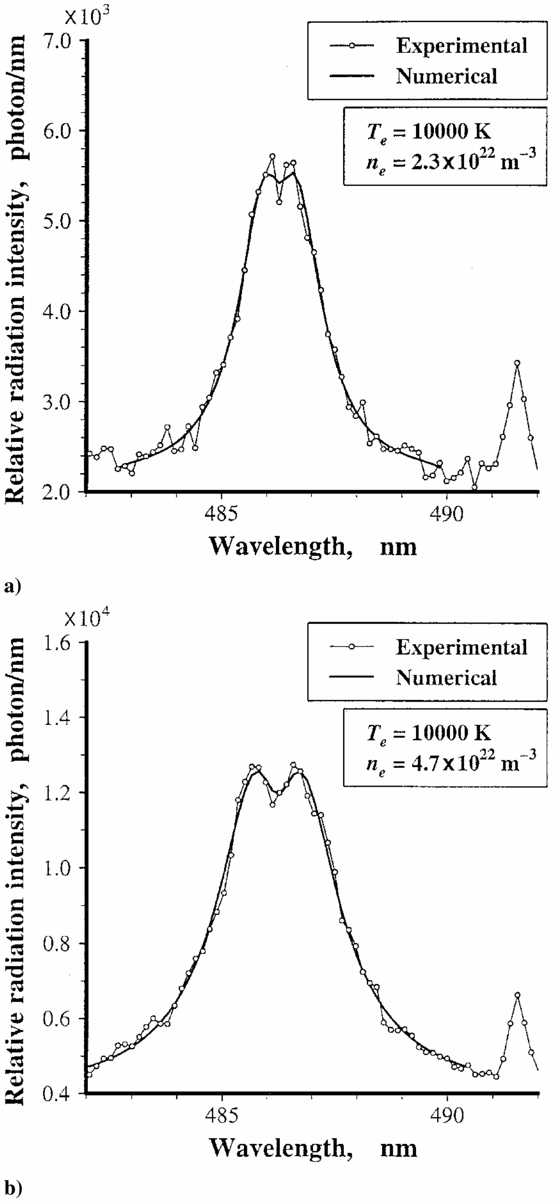

**Fig. 6 Numerical fit to observed H-$\beta$ profile: a) $L = 26.7 \pm 0.5$ mm, $V = 10.05 \pm 0.05$ km/s, $P_0 = 0.9$ torr and b) $L = 6.0 \pm 0.6$ mm, $V = 12.55 \pm 0.05$ km/s, $P_0 = 0.3$ torr; spectral resolution = 0.16 nm/pixel.**

## Comparison of Numerical Predictions with Experiment

### Numerical Model

To assess the thermochemical models widely used for reentry applications, numerical predictions obtained by these models are compared with the experimental results. Because the numerical models used here are well-known and described in detail in the literature (Refs. 1–4, for example), only a brief description of the models is given here. The numerical model is based on the two-temperature model, in which the translational and rotational energy modes are in equilibrium at the translational temperature, and the vibrational, electronic, and electron translational energy modes are in equilibrium at the vibrational temperature.[1] The parameters for translational–vibrational relaxation and the chemical reaction-rate coefficients are taken from Ref. 4. Internal energy of each chemical species and a set of equilibrium constants for chemical reactions are taken from Ref. 3.

Following a recommendation of Park,[3] the preferential dissociation model is used by setting the average vibrational energy lost at dissociation to be 0.3 × $D_0$, where $D_0$ is the dissociation energy measured from the vibrational ground state. On the other hand, the average electronic energy lost at ionization is assumed to be

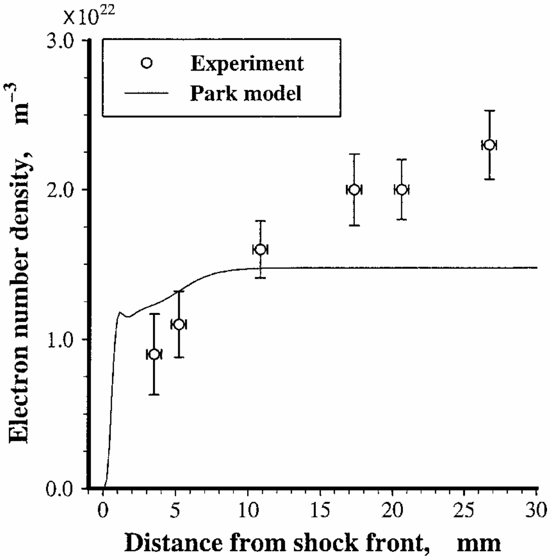

**a) $V = 10.05 \pm 0.05$ km/s, $P_0 = 0.9$ torr**

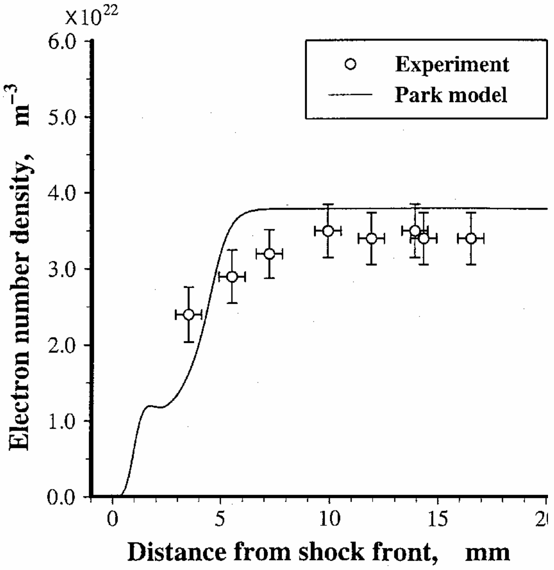

**b) $V = 11.01 \pm 0.05$ km/s, $P_0 = 0.55$ torr**

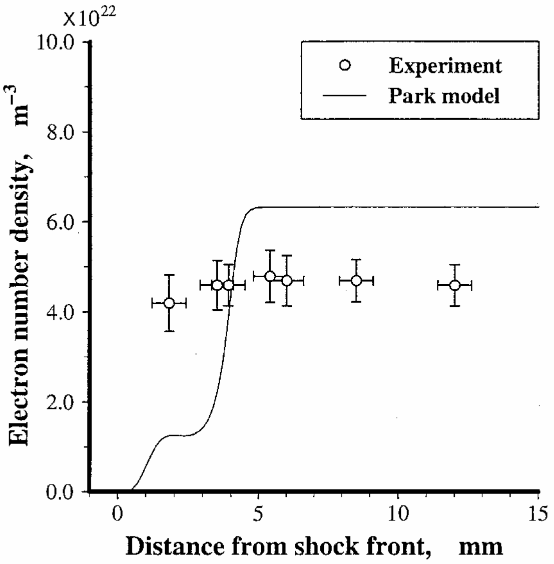

**c) $V = 12.55 \pm 0.05$ km/s, $P_0 = 0.3$ torr**

**Fig. 7 Variation of electron density behind the shock front.**

equivalent to the ionization energy measured from the electronic ground state. The geometrical mean temperature used to calculate dissociation-rate coefficients is given by the most general description $T_a = \sqrt{(TT_v)}$, as suggested in Ref. 4. The viscosity, the heat conductivity, and the mass diffusion flux are computed in a manner similar to that by Fertig et al.,[11] based on Hirschfelder's theory[12] by incorporating the ambipolar diffusion.[13] Collision integrals for collisions between charged particles are taken from Ref. 11, whereas the latest curve fitting of Capitelli et al.[14] is used for other collision integrals. The preceding models are used because they were found to numerically reproduce the vibrational temperatures measured in the previous experiment.[7]

## Results and Discussion

The calculated electron density is plotted as a solid curve in Figs. 7a–7c. For $V = 10.05$ km/s the calculated density is found to increase more quickly immediately behind the shock front than the measured density, as seen in Fig. 7a. However, because the accuracy of the measurement is degraded in this region as a result of a decrease in intensity of the H-$\beta$ line the numerical prediction is considered to be in good agreement with the experiment within a 10-mm distance from the shock front. At a distance further than 10 mm from the shock front, the measured density still increases gradually while the numerical result is in an equilibrium state. As shown in Fig. 2a, the total radiation intensity also increases gradually from 1–4 $\mu$s after the shock arrival, which corresponds to a distance of 10–40 mm from the shock front. The increase of the total radiation intensity suggests an increase of the temperature or the density in this region, both of which can increase the electron density.

A similar increase of the radiation intensity is also seen in Wilson's experiment[15] at the shock velocity of 9.5 km/s, which is almost the same velocity as our experiment. Park[4] attributed such an increase of the electron density to the existence of iron impurities contained in the test gas in Wilson's experiment. However, it might not be the case of our experiment because the shock tube is made of aluminum alloy to get rid of such impurities. We consider the gradual increase of the total radiation intensity is caused by a density increase (and a pressure increase correspondingly), which is brought about by an increase in thickness of the boundary layer in this region. The boundary-layer thickness $\delta$ can be estimated roughly by $\delta/L = \sqrt{(\nu/UL)}$, where $\nu$ is the kinematic viscosity and $U$ is the streaming velocity behind the shock wave. The right-hand side of this equation is of the order of $10^{-2}$ for $L = 40$ mm under the tested conditions, so that the boundary-layer thickness is of the order of 1 mm at $L = 40$ mm. Because the test section is 35.4-mm square in cross section, the boundary layer of 1-mm thickness on four sides of the flow channel results in a 10% decrease in the effective channel section for the undisturbed flow. Because this effect is not taken into consideration, the model cannot reproduce the experimental results in this region.

The electron density calculated for $V = 11.01$ km/s and $P_0 = 0.55$ torr is in good agreement with the experimental result, as seen in Fig. 7b. One reason for this agreement is that the ionization model used in this analysis is adjusted to the shock velocities below 11.3 km/s by Park.[4] In contrast, the electron density calculated for $V = 12.55$ km/s and $P_0 = 0.3$ torr shows that the trend is essentially different from the experiment immediately behind the shock front: the measured electron density increases much more quickly than the numerical prediction. This coincides with the fact that the ionization front is located at the close vicinity of the shock front as illustrated in Fig. 2b.

To account for this discrepancy between the calculated and the measured electron density immediately behind the shock front for $V = 12.55$ km/s, distributions of the calculated temperatures, chemical composition, and chemical reaction rates related with ionization are plotted in Figs. 8a, 8b, and 8c, respectively. From these figures it is understood that, in Park's chemical reaction model applied to pure nitrogen as the test gas, electrons are produced first by the associative ionization, $N + N \rightarrow N_2^+ + e$. When the resulting electron density increases adequately and the electronic temperature reaches a certain threshold value simultaneously, the electron-impact ionization,

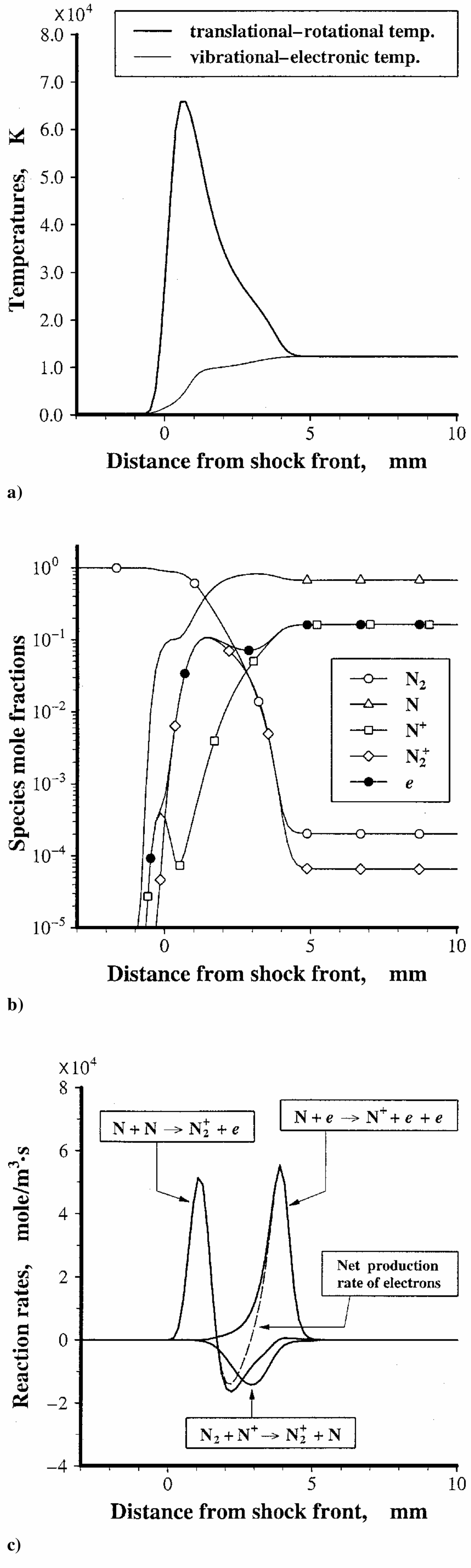

Fig. 8 Variation in a) temperatures, b) chemical composition, and c) chemical reaction rates behind the shock wave calculated by Park's model for $V = 12.55$ km/s and $P_0 = 0.3$ torr.

$N + e \rightarrow N^+ + e + e$, begins to contribute significantly to production of electrons in the form of the avalanche ionization.[3] Therefore, in order to predict the variation of the electron density accurately it is necessary to accurately describe 1) the associative ionization, 2) the relaxation of the electron temperature, and 3) the electron-impact ionization, provided that the ionization process of the Park model is essentially correct. Otherwise, another mechanism that can enhance the ionization should be taken into account under the tested conditions.

Even if we take account of several uncertainties in the Park model, the discrepancy between the measured and the calculated density cannot be resolved. For example, if we change the geometrical mean temperature to $T_a = T^{0.7} T_v^{0.3}$, which can enhance the ionization, the distance at which the test gas reaches an equilibrium state is calculated to be only slightly shorter behind the shock front. For another example, even though we use the three-temperature model where the electronic temperature is assumed not to be in equilibrium with the vibrational temperature,[3] the calculated electron density does not differ so much from the result shown in Fig. 7c.

A possible cause of the discrepancy between the measurement and theory is the rotational temperature nonequilibrium observed in the earlier experiment: the measured rotational temperatures are much lower than the translational temperature immediately behind the shock front under the tested conditions.[7] Because the rotational temperature is assumed to be in equilibrium with the translational temperature in the two-temperature model, the translational temperature can be underestimated. The electron temperature can also be underestimated because it is subject to relaxation with the translational temperature. Consequently, the rates of the associative ionization and the electron-impact ionization, which depend on the translational temperature and the electron temperature, respectively, are underestimated by the numerical model.

Another possible mechanism to increase the electron density is photoionization. The radiation distributed to ultraviolet and vacuum-ultraviolet wavelengths, in which photons have energy high enough to ionize molecular and atomic nitrogen, is known to become intense as the shock velocity increases above 12 km/s (Ref. 16) and can begin to play a more dominant role in ionization processes. The contribution of photoionization can also increase the electron temperature for the following reason: when electron-impact ionization is dominant, the electron temperature is not allowed to increase quickly because the translational energy of electrons is used to ionize atomic nitrogen. In contrast, when photoionization is dominant the electron temperature can increase more quickly because the electron energy is not necessary to produce electrons in photoionization. The increase of both the electron density and electron temperature is expected to trigger easily the avalanche ionization at a shorter distance from the shock front.

The deviation of the numerical prediction from the measured electron density distribution at $V = 12.55$ km/s suggests that the ionization model widely used for reentry applications loses its accuracy as the shock velocity increases above 12 km/s. It is necessary to improve the model by adjusting the parameters or by introducing other physical models to predict the quick ionization immediately behind the shock front. From a standpoint of designing the reentry vehicles, it is important to access an impact of the rapid increase of the electron density on the aerodynamic characteristics and the heating rate of the reentry vehicles, as far as the current ionization model is used to assess the flight environments in this velocity range.

## Summary

A simple and accurate technique to measure the electron density distribution behind a strong shock wave was developed. Using a free-piston double-diaphragm shock tube with nitrogen as the test gas, the time-frozen spectroscopy was performed simultaneously with the laser schlieren diagnostics to detect the shock front and to correlate the measured spectrum with the distance from the shock front. The present setup allows us to observe the time-frozen spectrum with high spatial resolution of ±0.6 mm at a shock velocity of 12 km/s.

The electron number density was determined by means of a line profile matching technique, using the H-$\beta$ line profile broadened and shifted by the Stark effect. The accuracy of the measured electron density is estimated to be within ±12% errors in general. The numerical predictions obtained by the thermochemical models widely used were compared with the experimental results. For the shock velocities of 10.05 and 11.01 km/s, good agreement is obtained between the measurement and theory, although ionization is seen to proceed a little more slowly in the experiment than in the numerical prediction.

At the shock velocity of 12.55 km/s, the electron density is found to increase significantly more rapidly behind the shock front in the experiment than predicted by the numerical model. The deviation of the numerical prediction from the experiment indicates that the ionization model widely used for reentry applications loses its accuracy as the shock velocity increases above 12 km/s and should be improved so that it can predict the rapid ionization immediately behind the shock front in this velocity range.

## Acknowledgment

The present work is partly supported by Grant-in-Aid for Encouragement of Young Scientists 11750791 at the Ministry of Education, Science, Sports and Culture, Japan.

## References

[1] Gnoffo, P. A., Gupta, R. N., and Shinn, J. L., "Conservation Equations and Physical Models for Hypersonic Air Flows in Thermal and Chemical Nonequilibrium," NASA TP-2867, Feb. 1989.

[2] Gupta, R. N., Yos, J. M., Thompson, R. A., and Lee, K. P., "A Review of Reaction Rates and Thermodynamic and Transport Properties for an 11-Species Air Model for Chemical and Thermal Nonequilibrium Calculations to 30,000 K," NASA RP-1232, Aug. 1990.

[3] Park, C., *Nonequilibrium Hypersonic Aerothermodynamics*, Wiley, New York, 1990, Chaps. 1–5.

[4] Park, C., "Review of Chemical-Kinetic Problems of Future NASA Missions, I: Earth Entries," *Journal of Thermophysics and Heat Transfer*, Vol. 7, No. 3, 1993, pp. 385–398; also AIAA Paper 91-0464, Jan. 1991.

[5] Gupta, R. N., Moss, J. N., and Price, J. M., "Assessment of Thermochemical Nonequilibrium and Slip Effects for Orbital Reentry Experiment (OREX)," NASA TM-111600, July 1996.

[6] Suzuki, K., Kubota, H., Fujita, K., and Abe, T., "Chemical Nonequilibrium Stagnation Ablation Analysis of MUSES-C Superorbital Re-Entry Capsule," *Journal of Spacecraft and Rockets*, Vol. 35, No. 3, 1998, pp. 407–409; also AIAA Paper 97-2489, June 1997.

[7] Fujita, K., Sato, S., Abe, T., and Ebinuma, Y., "Experimental Investigation of Air Radiation from Behind a Strong Shock Wave," *Journal of Thermophysics and Heat Transfer*, Vol. 16, No. 1, 2002, pp. 77–82; also AIAA Paper 98-2467, June 1998.

[8] Schott, L., "Electrical Probes," *Plasma Diagnostics*, edited by W. Lochte-Holtgreven, American Inst. of Physics, New York, 1995, Chap. 11, pp. 668–731.

[9] Griem, H. R., Kolb, A. C., and Shen, K. Y., "Stark Broadening of Hydrogen Lines in a Plasma," *Physical Review*, Vol. 116, No. 1, 1959, pp. 4–16.

[10] Griem, H. R., *Plasma Spectroscopy,* McGraw–Hill, New York, 1964, Chap. 4, pp. 64–104.

[11] Fertig, M., Dohr, A., and Fruhauf, H.-H., "Transport Coefficients for High Temperature Nonequilibrium Air Flows," AIAA Paper 98-2937, June 1998.

[12] Hirschfelder, J. O., Curtiss, C. F., and Bird, R. B., *Molecular Theory of Gases and Liquids*, Wiley, New York, 1954, Chap. 7, pp. 478–491.

[13] Devoto, R. S., "Transport Properties of Ionized Monatomic Gases," *Physics of Fluids*, Vol. 9, No. 6, 1966, pp. 1230–1240.

[14] Capitelli, M., Gorse, C., Longo, S., and Giordano, D., "Transport Properties of High Temperature Air Species," AIAA Paper 98-2936, June 1998.

[15] Wilson, J. F., "Ionization Rate of Air Behind High-Speed Shock Waves," *Physics of Fluids*, Vol. 9, No. 10, 1966, pp. 1913–1921.

[16] Fujita, K., Abe, T., and Suzuki, K., "Air Radiation Analysis of a Superorbital Reentry Vehicle," AIAA Paper 97-2561, June 1997.